Istraživanja i projektovanja za privredu
ISSN 1451-4117
DOI:10.5937/jaes0-45415
www.engineeringscience.rs

iipp publishing

Journal of Applied Engineering Science
Vol. 21, No. 4, 2023
Original Scientific Paper
Paper number: 21(2023)4, 1156, 1156-1170

NUMERICAL STUDY THE EFFECT OF AIR BARRIERS HEIGHT INSIDE THE AIR CONDITIONING DUCTING TO SATISFY THE REGULATION OF INDONESIA MINISTER OF TRANSPORTATION NUMBER 69 OF 2019

Fauzun Fauzun[1]*, Cahyo Wibi Yogiswara[1], Hifni Mukhtar Ariyadi[1], Muhammad Salim Taufiqurrahman[1], Aldy Franstanata Ritonga[1], Indro Pranoto[1], Rendianto Aginta Garingging[1], Fakhreza Areli[1], Rahma Kurnia Putra[1], Maulana Hafizh Al-Qadri[1], Afrizal Soffan Fatkhi[1], Rahardian Titus Nurdiansyah[2], Firdausa Retnaning Restu[2]

[1] Department of Mechanical and Industrial Engineering, Faculty of Engineering, Universitas Gadjah Mada, Jalan Grafika 2 Kampus UGM Yogyakarta, 55284, Indonesia
[2] Department of Engineering, Technology Division, PT. Industri Kereta Api (Persero) Jalan Yos Sudarso 71, Madiun, 63122, Indonesia

** fauzun71@ugm.ac.id*

The Indonesian smart hybrid light train is a train under development by the government and will operate in Makassar-Parepare, Indonesia track. The authors conducted a numerical study on CFD to investigate the air flow distribution inside the air conditioning ducting and the air velocity and air temperature distribution on Motor Engine and Compartment (MEC) car to achieve the passenger comfort criteria based on the regulation standard of Indonesia Minister of Transportation Number 69 of 2019. This study was conducted by simulating 5 variations of air barriers height inside the supply ducts. The input of air into the ducting has the parameters of mass flow rate, static temperature, static pressure, and density with the values of 1 kg/s, 20 °C, 1 atm, and 1.2 kg/m^3, respectively. The simulation results show that variation E is the best design which generated the average air velocity and air temperature distribution in the executive passenger cabin with the values of 0.25 m/s and 21.91 °C, respectively. Meanwhile, the other 4 variations did not satisfy the standard. The results also show that the ducting geometry can accommodate the air temperature difference on the MEC car that does not exceed 1.5 °C and the air supply is sufficient from the air conditioner unit to the driver room.

Keywords: KRHKC, CFD, ducting, passenger comfort, air barrier

1 INTRODUCTION

The smart hybrid light train or "*Kereta Ringan Hybrid dan Kereta Cerdas*" (KRHKC) is a train developed by the Indonesian government. The train is planned to operate with the operational route of Makassar – Parepare with a mileage of about 154 km. With this mileage, this train is classified as an intercity train where passenger comfort is the main concern. Thermal comfort has always been a primordial necessity in the life of human beings [1]. Thermal comfort or the indoor air temperature of a building directly effects the consumption of energy from air conditioning [2]. Several parameters that affect the level of passenger comfort based on environmental factors are vibration, noises, air temperature, pressure, and lighting [3]. With the concept of high-speed trains, it is necessary to have tightly sealed compartments of train cars where air temperature parameters need to be considered in more depth. This is because the condition of the room with tightly closed, and the presence of passengers makes the air temperature in the room rise. One of the reasons for air temperature increases is the heat flux value of the passengers [4]. This requires air control in the passenger room to ensure passenger comfort can always be maintained [5]. In controlling air distribution in train cabins, one of the major concerns is determining the design of air conditioning ducting. With the compact design of the train carriages and the optimization of each component in the carriages, the space for air conditioning ducting is limited. Moreover, the problem of distributing cold air into the driver room which must pass through the engine room with a heat source from engine operation, is a challenge that needs to be resolved so that the flowing cold air does not experience a significant air temperature drop.

Optimizing heating, ventilation, and air conditioning (HVAC) systems is crucial for improving energy efficiency in buildings due to their significant energy consumption. However, developing more advanced optimization techniques and energy-efficient HVAC systems is necessary to achieve sustainable and efficient building operation. In addition, optimized air conditioning ducting can also play a significant role in increasing energy efficiency and improving occupant comfort within buildings [6]. Hesser and Widdowson (2016) stated that comfort criteria for passenger rooms can be reviewed from 3 aspects there are maximum air velocity, overall room temperature, and air temperature differences at every point [7]. In Indonesia, the standard for thermal comfort of a high-speed train is regulated by the Indonesia Minister of Transportation number 69 of 2019 where the air temperature difference in each passenger seat may not exceed 1.5 °C and the air flow velocity hitting the passenger may not exceed 0.5 m/s [8].

This research discussed the numerical study of air flow and distribution in KRHKC ducting for the executive passenger cabin and the driver room. The research was conducted by simulating 5 different variations of the air barriers height inside the supply ducts. Variations are made by changing the height of the air barriers inside the

ducting to obtain the best distribution of air flow in each diffuser entering the executive passenger cabin. A heat source in the executive passenger cabin was generated by human bodies and window glasses. Therefore, the research conducted focuses on knowing the best air flow temperature and air flow velocity distribution (as standard) values between 5 variations of the air barriers height inside the ducting.

2 RESEARCH METHODS

2.1 Governing Equation

Governing equation is an equation used to complete the simulation process and numerical analysis in CFD (Computational Fluid Dynamics) [9]. CFD approach is a cost-effective alternative and less time-consuming. The solution obtained from CFD simulations is largely within the acceptable range [10]. The governing equation consists of basic fluid mechanics equations such as the equation for the conservation of mass, conservation of momentum, and conservation of energy as shown in Eqs. (1), (2), and (4) respectively. Stress tensor can be solved using Eq. (3). These equations are changed from the form of partial differential equations to algebraic equations by ANSYS Fluent, so they can finally be solved in numerical calculations [11].

$$\frac{\partial \rho}{\partial t} + \nabla.(\rho \vec{v}) = S_m \tag{1}$$

$$\frac{\partial}{\partial t}(\rho \vec{v}) + \nabla.(\rho \vec{v}\vec{v}) = -\nabla p + \nabla.(\bar{\bar{\tau}}) + \rho \vec{g} + \vec{F} \tag{2}$$

$$\bar{\bar{\tau}} = \mu \left[(\nabla \vec{v} + \nabla \vec{v}^T) - \frac{2}{3} \nabla.\vec{v} I \right] \tag{3}$$

$$\frac{\partial}{\partial t}(\rho E) + \nabla.\left(\vec{v}(\rho E + p)\right) = -\nabla.\left(\sum_j h_j J_j \right) + S_h \tag{4}$$

The $k-\omega$ model use two transports to solve the turbulence model. This modeling is based on the transport model equation for turbulence kinetic energy (k) and specific dissipation rate (ω) as shown in Eqs. (5) and (6). This model has the advantage of being able to display the flow transition from laminar flow to turbulent flow. Menter, Sechner, and Matyushenko (2021) developed the $k-\omega$ SST model to effectively combine the ability of the $k-\omega$ model around the wall, with the ability of the $k-\varepsilon$ model in the freestream area (far from the wall or high Reynolds number) [12]. By combining these two models, the weaknesses of the $k-\omega$ model in the form of sensitive results on free streams and on flows near walls at low Reynolds numbers can be overcome by the $k-\omega$ SST model, so that the turbulence model is more accurate and reliable for a wider range of flow regimes.

$$\frac{\partial}{\partial t}(\rho k) + \frac{\partial}{\partial x_i}(\rho k u_i) = \frac{\partial}{\partial x_j}\left(\Gamma_k \frac{\partial k}{\partial x_j} \right) + G_k - Y_k + S_k \tag{5}$$

$$\frac{\partial}{\partial t}(\rho \omega) + \frac{\partial}{\partial x_i}(\rho \omega u_i) = \frac{\partial}{\partial x_j}\left(\Gamma_\omega \frac{\partial \omega}{\partial x_j} \right) + G_\omega - Y_\omega + D_\omega + S_\omega \tag{6}$$

2.2 Numerical Simulation Methods

The method used in this research is CFD simulation using ANSYS Fluent 2020 R2 software. The schematic flow of the research carried out can be seen in Figure 1. The CFD simulation in this research used three stages:

- Pre-Processing

  The first stage must be done to make the geometry and to define the boundary conditions. In this research, geometry was made using the Autodesk Inventor Professional 2022 software. The geometry was divided into a certain number of grids that are called meshing. Dividing the continuous fluid domains into discrete domains in the form of small cells aims to make numerical processes applicable to the fluid equations. The smaller the cell size will make greater the number of cells, the results from the simulation using CFD will be more accurate, but the computation will take time longer.

- Processing

  The processing stage is solving analytical problems using equations that are suitable for the problems that are analyzed with numerical methods. This stage began by determining the values and conditions that are needed for the purposes of numerical calculations. CFD simulation was continued with the process of iteration until convergent results were obtained. The sequence of steps in this stage was defining the

boundary conditions, defining the fluid properties, defining the set-up, and defining the iteration number and optimal convergence limits.

– Post-Processing

This is the last stage in the simulation process where the calculated data was obtained in various output forms, such as images, graphics, and animation. The data taken at this stage were the distribution of air velocity and air temperature along the train.

2.3 Computational Domain

Motor Engine and Compartment (MEC) car consists of several parts, namely mascara, driver room, engine room, and executive passenger cabin. The complete design of the MEC car is shown in Figure 2. The mascara and engine room design sections were not used in the computational domain of CFD simulation. The computational domain is shown in Figure 3, which consists of a driver room, 2 supply ducts, 1 return duct, and an executive passenger cabin.

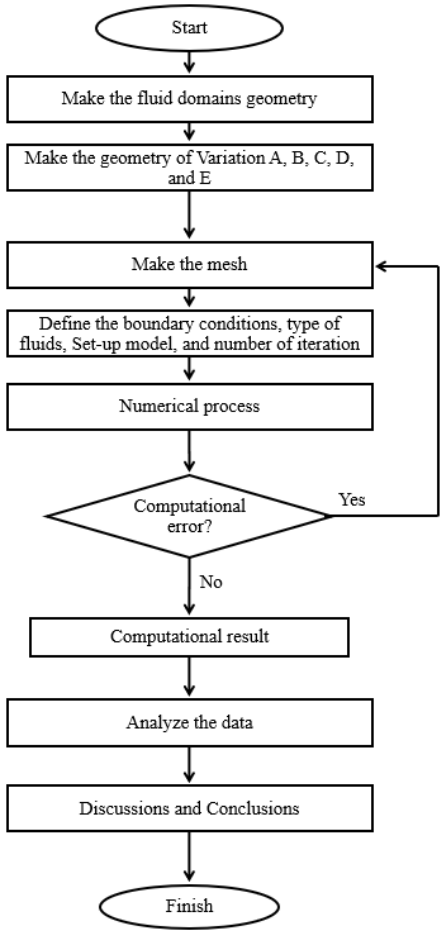

Fig. 1. Research flow scheme

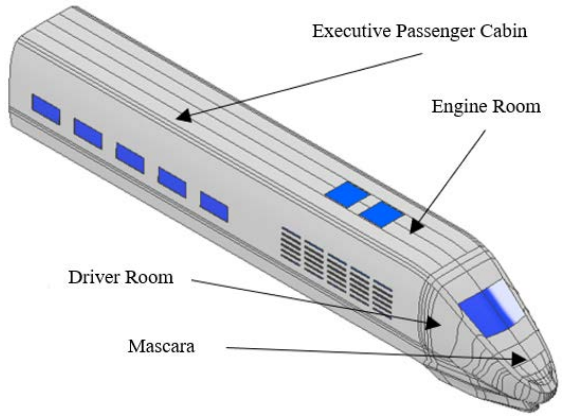

Fig. 2. Motor Engine and Compartment (MEC) car

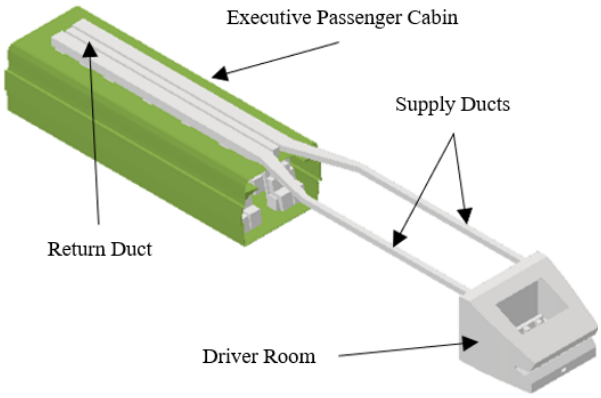

Fig. 3. Computational domain of MEC car

2.4 Boundary Conditions and Material Parameters

In this research, the air came from an Air Conditioner (AC) unit which has cooling capacity, mass flow rate, and working air temperature of 35 kW, 1 kg/s, and 20 °C respectively. These values were used as boundary conditions of air input parameters inside the ducting. CFD can offer a quick and cost-effective means of study with the advantage of having large flexibility in the geometry and boundary conditions [13].

The glass material used in this KRHKC research was divided into 2 types based on the placement position, driver room and executive passenger cabin. The glass for the driver room was located on the front windshield of mascara, while the glass for the executive passenger cabin was located on the side window. The glasses are shown in Figure 4 and Figure 5. The glass of the side window of the executive passenger cabin consists of 7 layers of material and the glass of front windshield of mascara consists of 5 layers of material. Meanwhile, the ducting was manufactured with galvanized steel material, and it was insulated with EVA foam throughout the engine room. The authors used the shell conduction feature in ANSYS Fluent to input the material parameters of each layer of the glasses and the ducting. Detailed specifications of material parameters of the glasses and ducting are shown in Table 1.

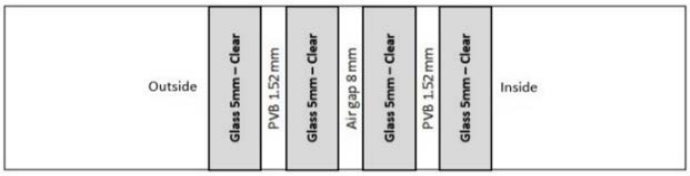

Fig. 4. Side window of the executive passenger cabin

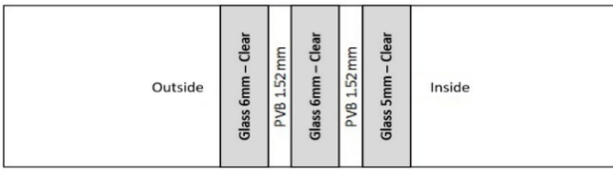

Fig. 5. Front windshield of mascara

Table 1. Material parameters of cabin glass, mascara glass, and ducting [4], [14]

Properties	Unit	People	Cabin glass						
			L1 - glass	L2 - PVB	L3 - glass	L4 – air gap	L5 - glass	L6 - PVB	L7 - glass
ρ	kg/m^3	1038.8	2520	1120	2520	1.204	2520	1120	2520
C_p	J/kg K	3341.3	753	1850	753	1.0035	753	1850	753
k	W/m K	0.62	0.96	0.2	0.96	1.4	0.96	0.2	0.96
T	°C	36	38	38	38	38	38	38	38
$q"$	W/m^2	56.52	-	-	-	-	-	-	-
t	m	5×10^{-6}	5×10^{-3}	1.52×10	5×10^{-3}	8×10^{-3}	5×10^{-3}	1.52×10^{-3}	5×10^{-3}
h	W/m^2 K	-	15	15	15	15	15	15	15

Properties	Unit	Mascara glass					Ducting	
		L1 - glass	L2 - PVB	L3 - glass	L4 – PVB	L5 - glass	L1 – Galvanized steel	L2 – EVA foam
ρ	kg/m^3	2520	1120	2520	1120	2520	7800	30
C_p	J/kg K	753	1850	753	1850	753	470	1400
k	W/m K	0.96	0.2	0.96	0.2	0.96	52	0.038
T	°C	38	38	38	38	38	34	34
$q"$	W/m^2	-	-	-	-	-	-	-
t	m	5×10^{-3}	1.52×10^{-3}	6×10^{-3}	1.52×10^{-3}	6×10^{-3}	1×10^{-3}	1×10^{-2}
h	W/m^2 K	15	15	15	15	15	15	15

2.5 Air Barrier Variation

There are 5 variations of air barriers height in this research. The ducting geometry consists of 2 supply ducts and a return duct. Each supply duct has 6 diffusers and 6 air barriers which are placed inside the supply duct. The diffuser numbers 1,3,4, and 6 have air grill inside, whereas the diffuser numbers 2 and 5 do not. The presence of air grill inside the diffuser is the same for all 5 variations. Meanwhile, the return duct has no air barriers applied inside. This research was started by using a ducting design without air barriers (variation A) as a baseline design. After that, optimization was done by using the air barriers with the variations of height. Detail of the variation in air barrier heights used in this research are shown in Table 2. Details of the ducting and air barriers drawing are shown in Figure 6.

Table 2. Variation of air barriers height

Variations	Air barriers height (mm)					
	1	2	3	4	5	6
A	Without air barrier					
B	40	40	40	40	40	40
C	60	60	60	60	60	60
D	80	60	60	40	60	50
E	80	68	60	48	60	56

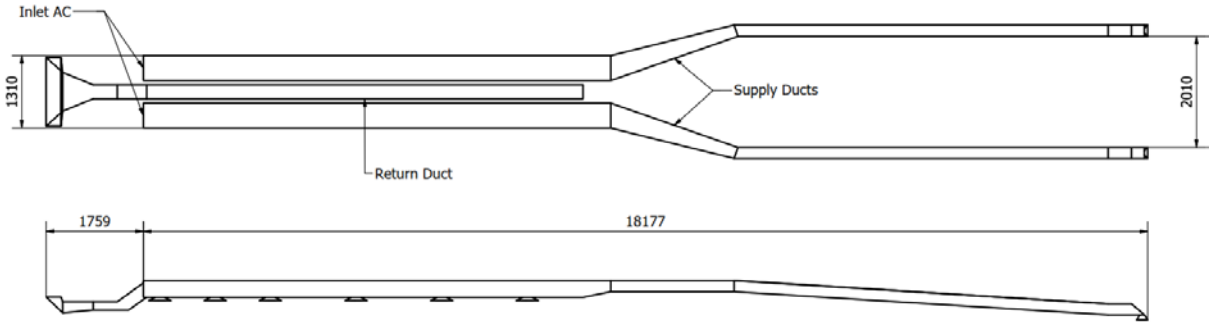

(a)

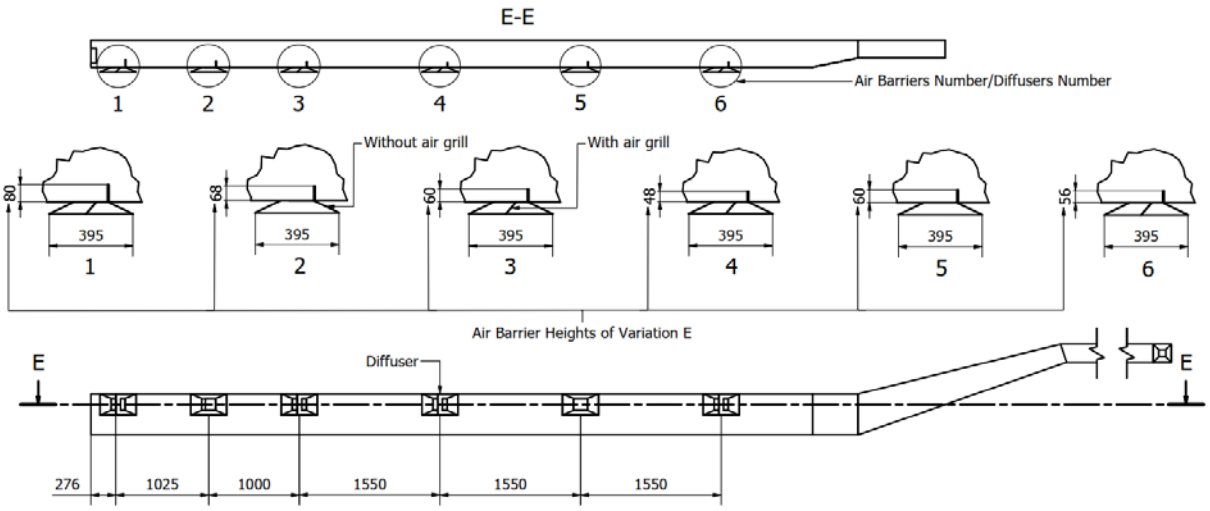

(b)

Fig. 6. (a) Top and side view of ducting and (b) Details of diffusers and air barriers

2.6 Meshing

Meshing was done by using a mesh size of 12 mm for human bodies, 40 mm for the walls of the engine room and glass, and 200 mm for the overall mesh size. So that the mesh has a total of 37,913,274 cells, 53,462,277 nodes, and has average skewness and orthogonal quality values of 0.22902 and 0.76969, respectively. These values show that the average skewness was excellent, and the average orthogonal quality was very good [9] [15]. The results of the mesh model geometry are shown in Figure 7.

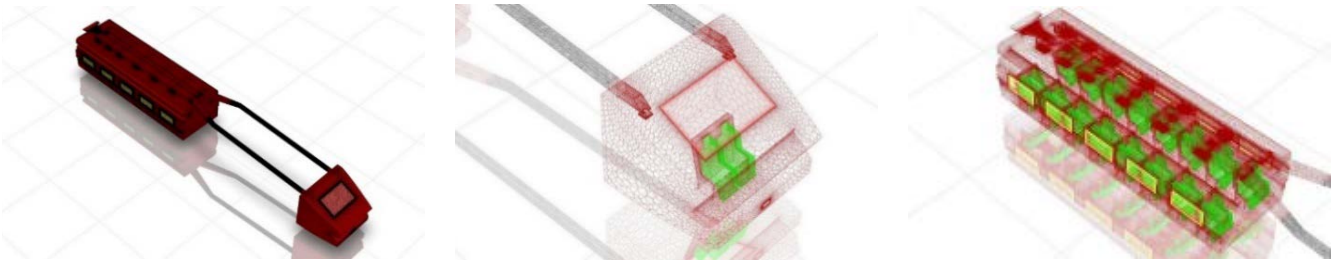

(a) (b) (c)

Fig. 7. Mesh models of (a) MEC car, (b) Driver room, and (c) Executive passenger cabin

2.7 Computational Set-Up

Computational set-up was done at a steady-state condition with coupled solution method. The coupled solution method can be used to solve the equation of conservation of mass, momentum, and energy simultaneously. These equations are non-linear equations which require iterations repeatedly before a convergent solution is obtained. Detailed setting information of the method used as shown in Table 3.

Table 3. Computational set-up

Model	Setting	Pressure Velocity Coupling	Setting	Discretization Scheme	Setting
Space	3D	Setup Condition	Default	Pressure	Second order
Time	Steady	Type	Coupled	Momentum	Second order upwind
Gravity	Enabled, 9.81 m/s^2	Pseudo transient	Yes	Turbulent kinetic energy	Second order upwind
Viscous	$k-\omega$ SST turbulence model	Explicit momentum under-relaxation	0.5	Specific dissipation rate	Second order upwind
Heat transfer	Enabled	Explicit pressure under-relaxation	0.5	Energy	Second order upwind

3 RESULT AND DISCUSSION

In this chapter, the authors presented a discussion of the results of air flow inside the ducting, air velocity and temperature in the executive passenger cabin. The air flow results inside the ducting will be presented with the projection of the air velocity vector around the air barriers, while the air velocity and air temperature results in the executive passenger cabin will be presented with the contours of the predetermined plane. The discussion of the

results of air velocity and air temperature in the executive passenger cabin is used to strengthen the discussion of air flow resulting from inside the ducting.

3.1 Air Flow Inside the Ducting

In this sub-chapter, the authors presented the projection of the air velocity vectors inside the ducting from 5 variations as described in Table 2. Figure 8 shows the results of the air velocity vectors projection taken from the plane that is exactly in the middle of the ducting. From Figure 8, the authors wanted to explain how the effect of air barriers height is on the flow of air from the ducting that goes out into the executive passenger cabin.

The order of the air barriers numbers is shown in Figure 8 (a), from order number 1 to number 6. The red arrows indicated a high air velocity vector (0.5 m/s), while the dark blue arrows indicated a low air velocity vector. Of the five variations A to E, almost no significant difference was found. However, there were 2 air barriers that seem to really have an impact on each variation, namely air barriers number 2 and 5. From the five variations in Figure 8, air barrier number 2 produced a high air velocity vector and hit the passenger seat right underneath. Variation A showed the most air velocity vectors in that area, while variation E showed the fewest air velocity vectors in that area.

For air barrier number 5, it gave different air velocity vectors results for each variation. For variation A, air barrier number 5 didn't produce too many air velocity vectors hitting the passenger seat underneath. In variations B and C, it can be said that the results of the air velocity vectors from air barrier number 5 were right about the passenger's head. For variation D, the results of the air velocity vectors even spread to the 2 passenger seats underneath. For variation E, the results of the air velocity vectors were more towards the back of the passenger seat underneath.

The resulting air velocity vectors phenomenon at air barrier points number 2 and number 5 was probably because there were no air grills at these two points. An explanation of the air grills had been shown in Figure 6 (b). The absence of air grills at these two points might cause the air flow from inside the ducting to be directly distributed in large quantities to the executive passenger cabin, causing the passenger seats underneath to get high air velocity. Therefore, in the next sub-chapter the authors will review in more detail the air flow conditions that occurred in air barrier number 2 and 5 for each variation. This aim was to further ensure that air barrier numbers 2 and 5 are the most influential points on the results of the air velocity vectors inside the ducting.

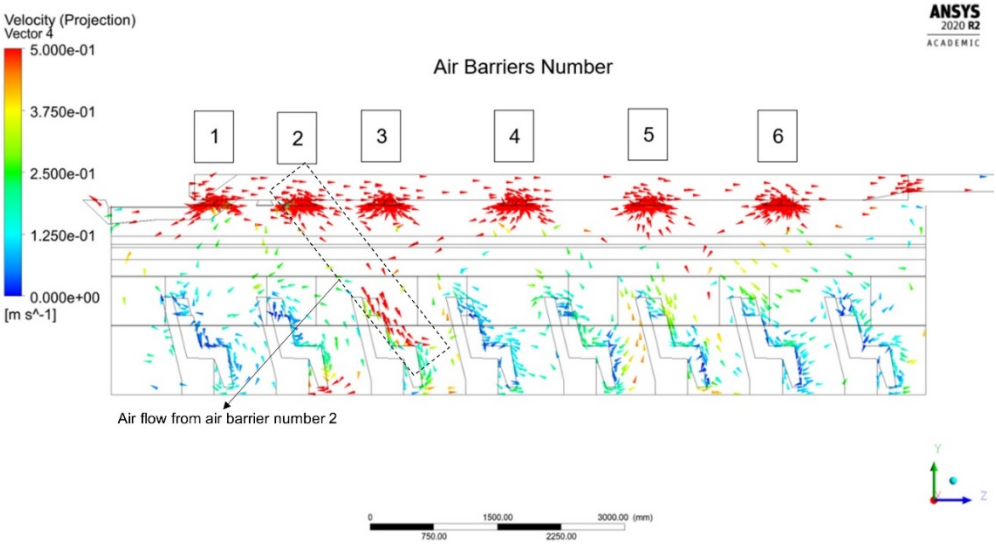

(a)

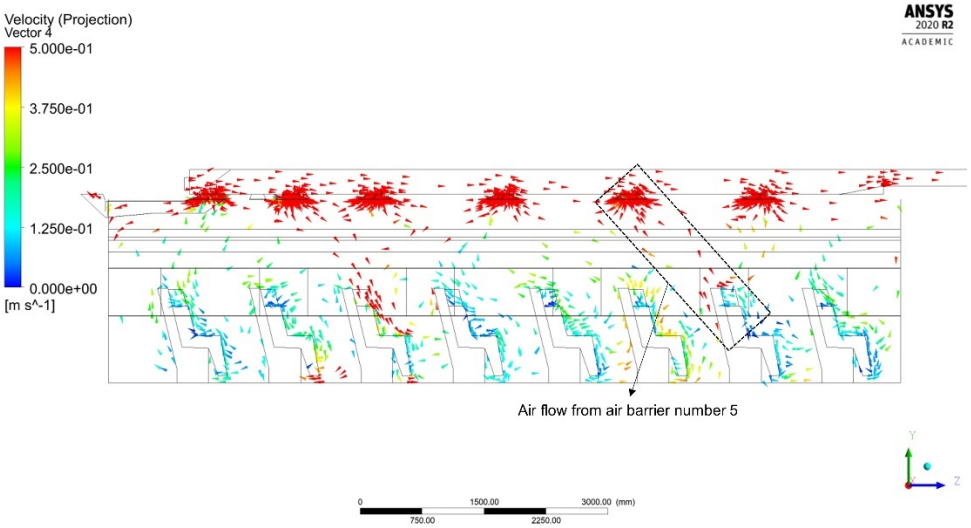

(b)

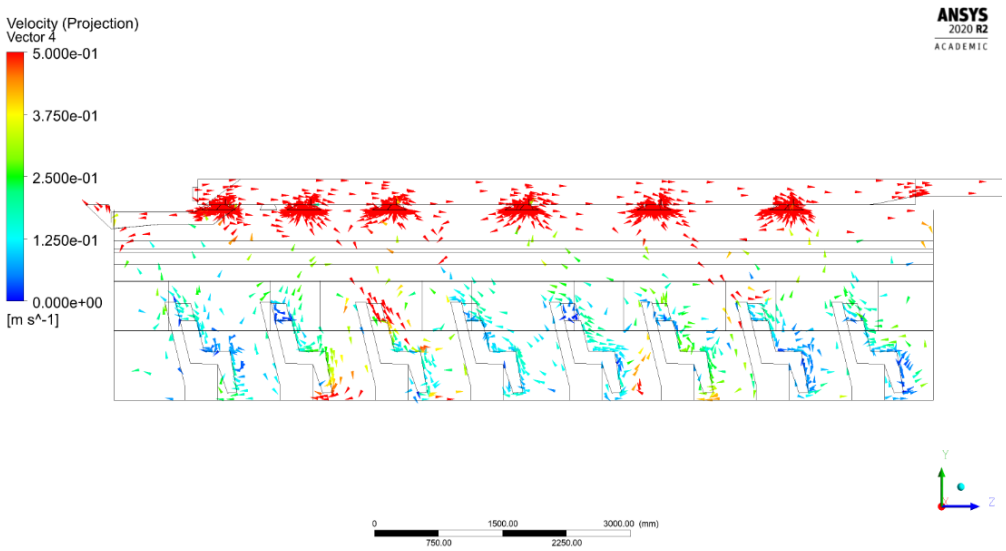

(c)

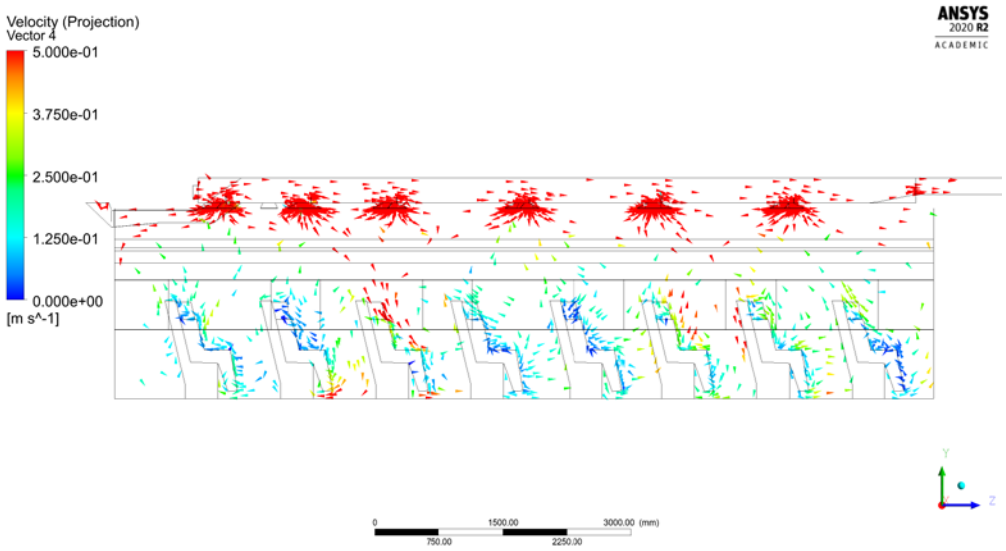

(d)

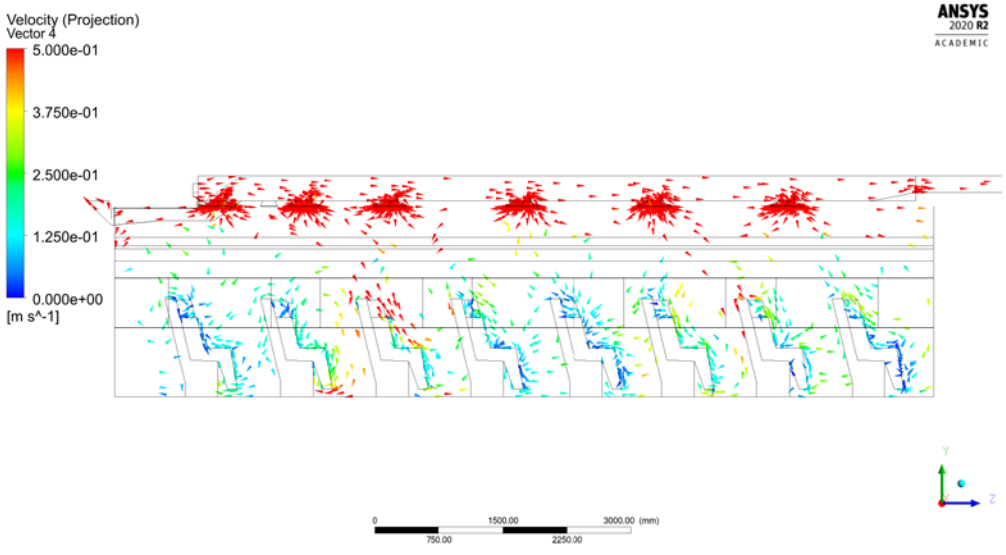

(e)

Fig. 8. Air velocity vector projection of ducting plane for (a) Variation A, (b) Variation B, (c) Variation C, (d) Variation D, and (e) Variation E

Next, the authors presented Table 4 to show the detailed phenomena that occur in air barriers number 2 and number 5. However, to show a sufficiently visible difference, the authors will compare the results of the air velocity vectors on the air barrier number 1 and number 2. This was due to air barrier number 1 containing air grill, while air barrier number 2 did not contain air grill. Thus, it was hoped that the results of the air velocity vector images at these 2 points

will give a clearer difference. Table 4 showed the results of the air velocity vector at air barrier points number 1 and number 2 for each variation A to E.

In Table 4, the presence of air grills in air barrier number 1 influenced the breakdown of air flow. The air flow was split because of hitting the walls of the air grill and caused a stream that spreads in random directions. After the air flow hit the air grill, there was a low-speed air velocity that led to the executive passenger cabin, marked with a green vector projection. Air grill also caused reversed flow which made the air flow that has already exited the diffuser enter again and hit the air flow that is still in the diffuser, marked by a blue vector projection. This phenomenon occurred for all variations A to E with almost uniform air velocity vector projections.

Meanwhile, in air barrier number 2 which did not have air grills, the air flowed will immediately flow quickly from the diffuser to the executive passenger cabin. This was indicated by the red projection vector. This was what might cause the air flow to flow at high velocity towards the passenger seat below, as described in Figure 8.

Thus, referring to the results listed in Table 4, it can be said that the presence of air grills in the diffuser can cause the air flow to spread more evenly before hitting the passenger seats underneath. Meanwhile, the absence of air grills will cause air flow to flow quickly towards the passenger seat underneath. This answered the phenomenon related to air flow in air barrier number 2 and number 5 which produced the highest air velocity vector. Henceforth, the authors will discuss the air flow that occurred in the executive passenger cabin to show the effect of the height of the air barrier inside the ducting on the distribution of air velocity and air temperature that occurs in the executive passenger cabin.

Table 4. Comparison of the vector velocity projection of air barrier number 1 and 2

Variations	Air Barrier Number 1	Air Barrier Number 2
A	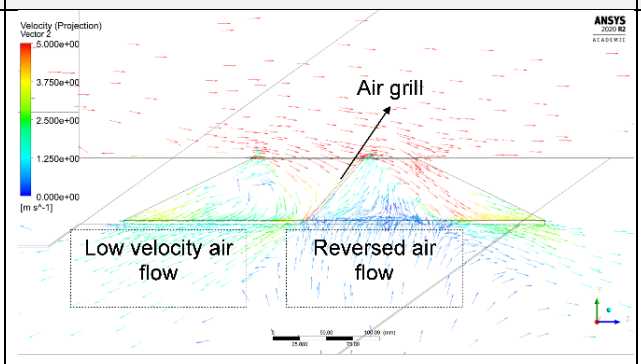	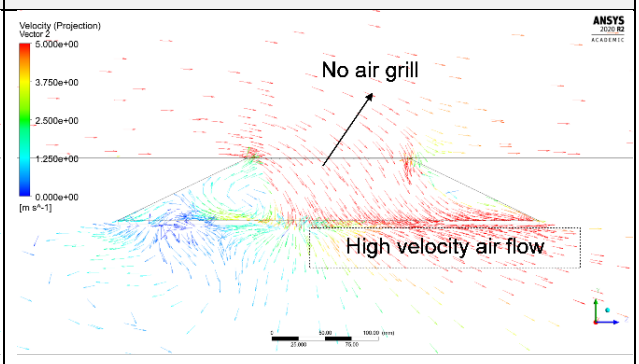
B	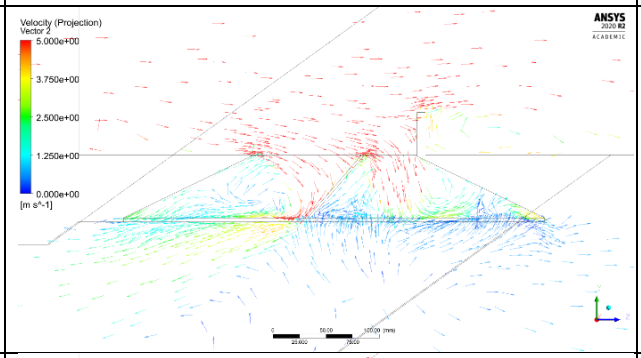	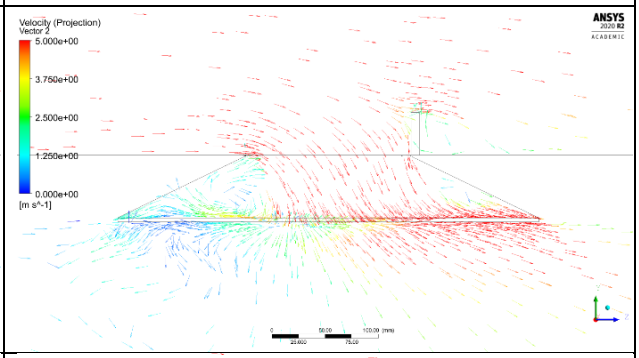
C	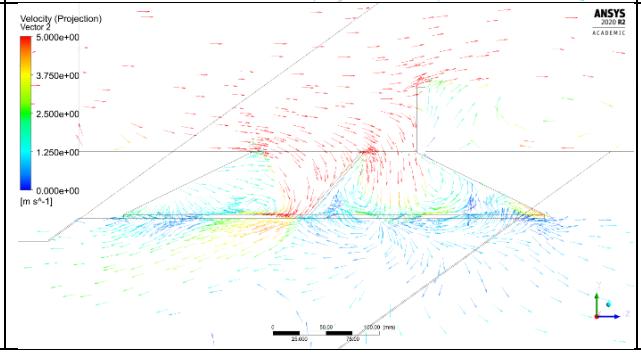	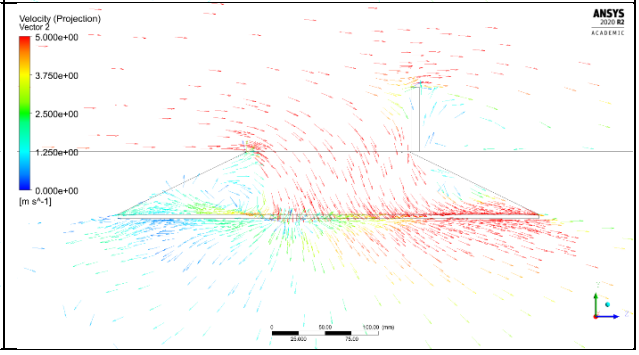

Variations	Air Barrier Number 1	Air Barrier Number 2
D	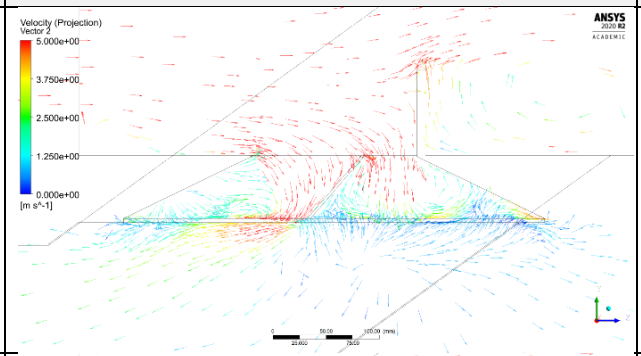	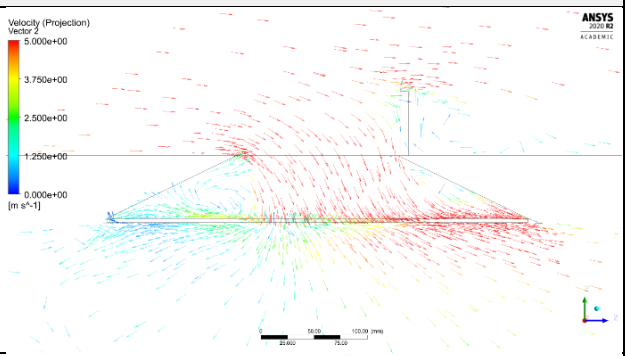
E	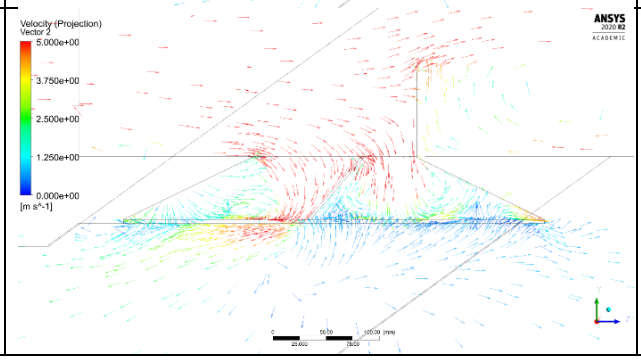	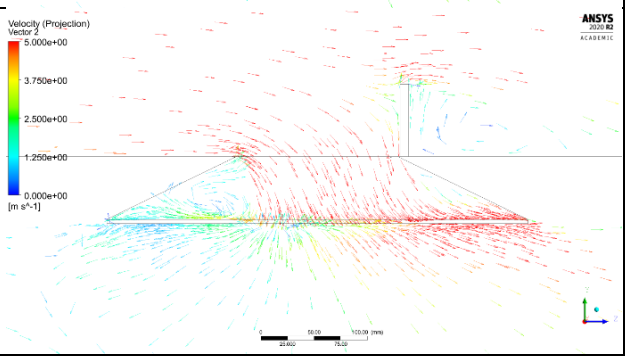

3.2 Air Velocity Distribution and Contours

In this section, the authors presented plotting points of the computational domain in the executive passenger cabin. It can be seen in Figure 9. It consists of the distance from the rear wall to the front wall in each meter. These plotting points were used to obtain the air temperature values in each meter. While the air velocity values were obtained by making a plane with the height of 1.2 meters from the floor as written in the regulation standard [8].

The air velocity distribution in the executive passenger cabin is shown in Figure 10. The figure contains a graphical plot of the air velocity distribution values for the 5 variations in air barrier heights inside the ducting by taking samples at several points at a height of 1.2 meters from the floor in the executive passenger cabin. The height of the air velocity plane and the plotting points of the executive passenger cabin were described in Figure 9. It can be observed that there was a very significant increase in the third passenger seat area, or at a plotting point of 3 meters, where the air velocity exceeds the standard 0.5 m/s for all air barriers height variations. This was because the location of this passenger seat is exactly placed under the diffuser which was used to circulate cold air into the executive passenger cabin. The air velocity limit of 0.5 m/s is shown by the horizontal dotted line in Figure 10.

Figure 11 shows the air velocity contours of the simulation results of all variations A, B, C, D, and E, respectively. It can be seen in all variations that the air velocity value in the driver room exceeded the specified standard. As for the executive passenger cabin, several points still had air velocity above 0.5 m/s. But overall, the air velocity was quite even. Based on the result of the graph in Figure 10, variation C produced the worst air velocity distribution because there was the highest significant increase of air velocity value in third passenger seats. The best result of air velocity distribution is shown in variation E, even though there was an increase of air velocity value in third passenger seats, but the air temperature value afterwards was quite even and below 0.5 m/s.

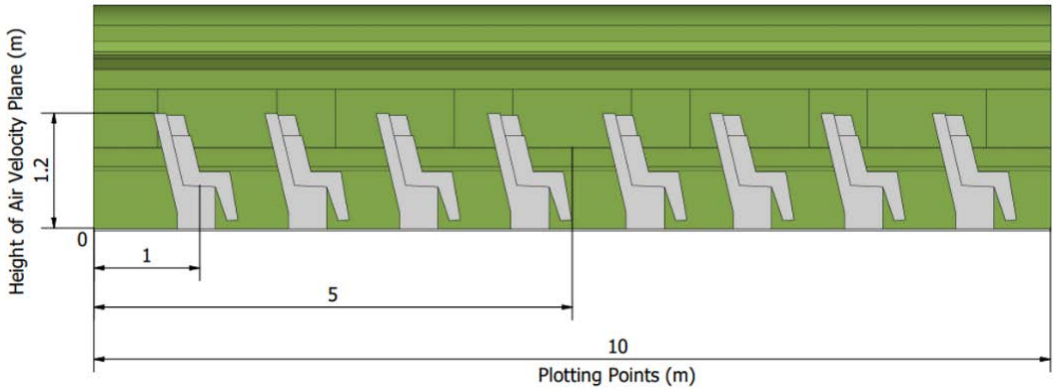

Fig. 9. Plotting points of computational domain in the executive passenger cabin

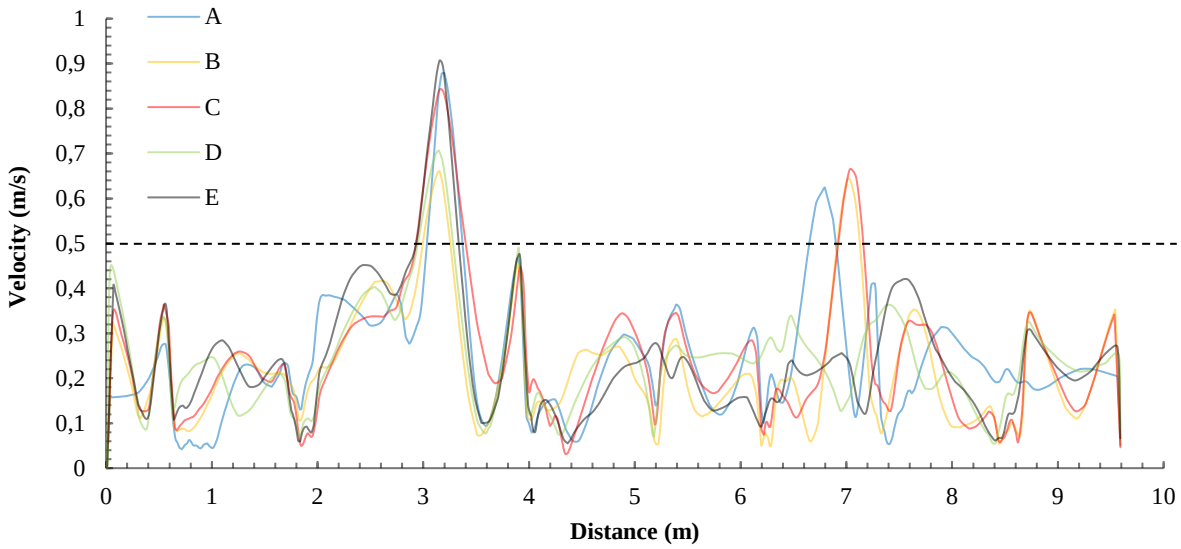

Fig. 10. Air velocity distribution in the executive passenger cabin

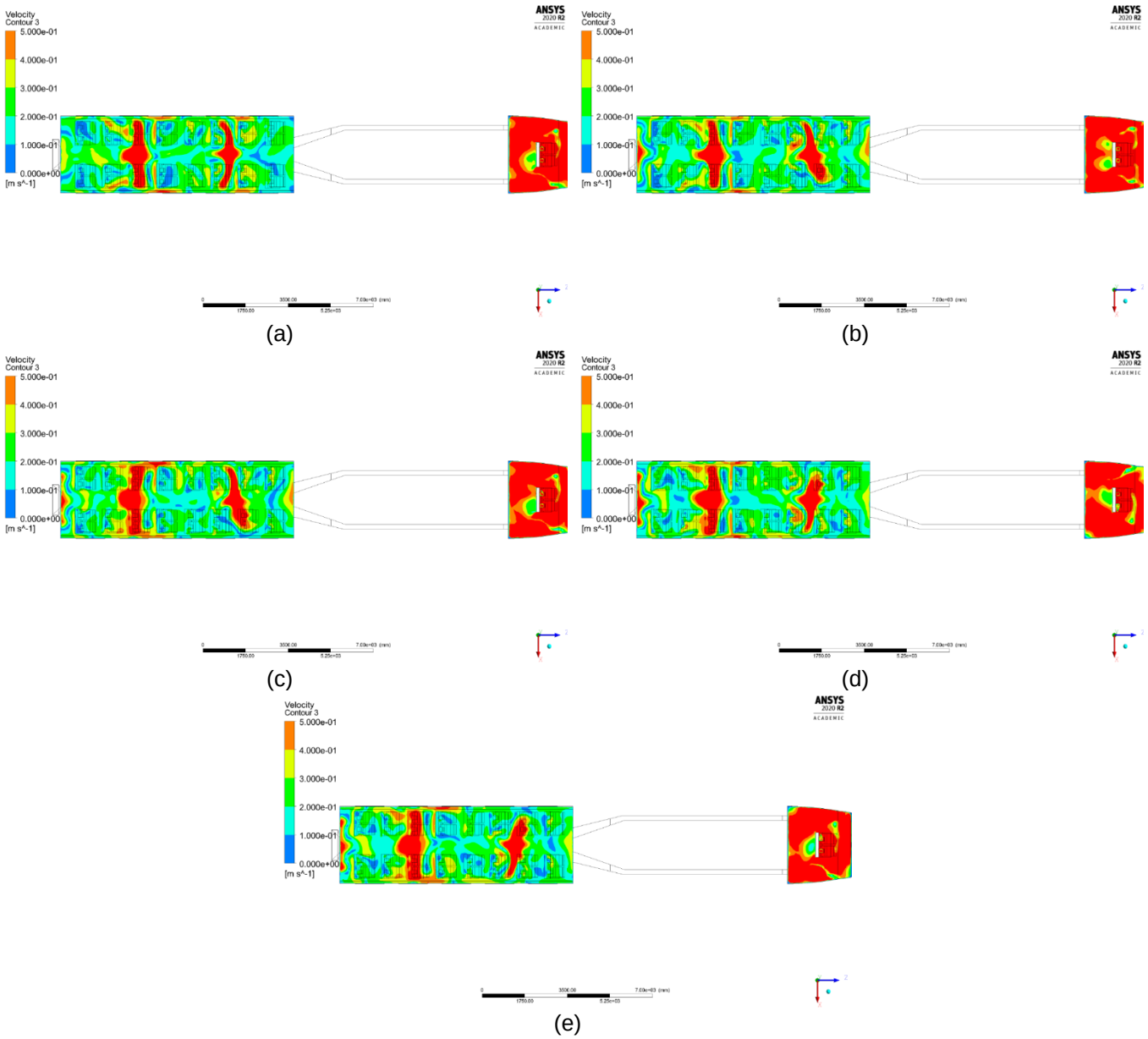

Fig. 11. Air velocity contours for (a) variation A, (b) variation B, (c) variation C, (d) variation D, and (e) variation E

3.3 Air Temperature Distribution and Contours

Air temperature distribution in the executive passenger cabin is shown in Figure 12. The figure contains a graphical plot of the air temperature distribution values for the 5 variations in air barriers height inside the ducting. The limit value of the air temperature difference is shown by the horizontal dotted line. According to the regulation standard, the value of air temperature difference should not exceed 1.5 °C.

Figure 13 and Figure 14 show the air temperature rendering and contours of the simulation results for variations A, B, C, D, and E, respectively in isometric and side views. From the results of the air temperature rendering, all variations showed that the air flow from the AC unit was sufficient to the driver room with an average air temperature value below 23 °C. Variations A and B showed very low air temperature contours in the rear passenger seats, or from plotting points of 0 to 3 meters, with air temperature values below 21 °C. Variation C showed very high air temperature contours in the middle to the front passenger seats, or from a plotting point of 5 to 10 meters, with an air temperature value above 25 °C. Variations D and E showed an even air temperature contour throughout the executive passenger cabin. From the results of the graph in Figure 12, the E variation was better than the D variation due to the difference in air temperature value of 1.36 °C and it met the regulation standard.

From the results of these air temperature distribution, it can be stated that the variation E produced the best air temperature distribution, while the variation C produced the worst air temperature distribution. These two variations will be compared with the results of the air velocity vector on the passenger plane closest to the window in Figure 15.

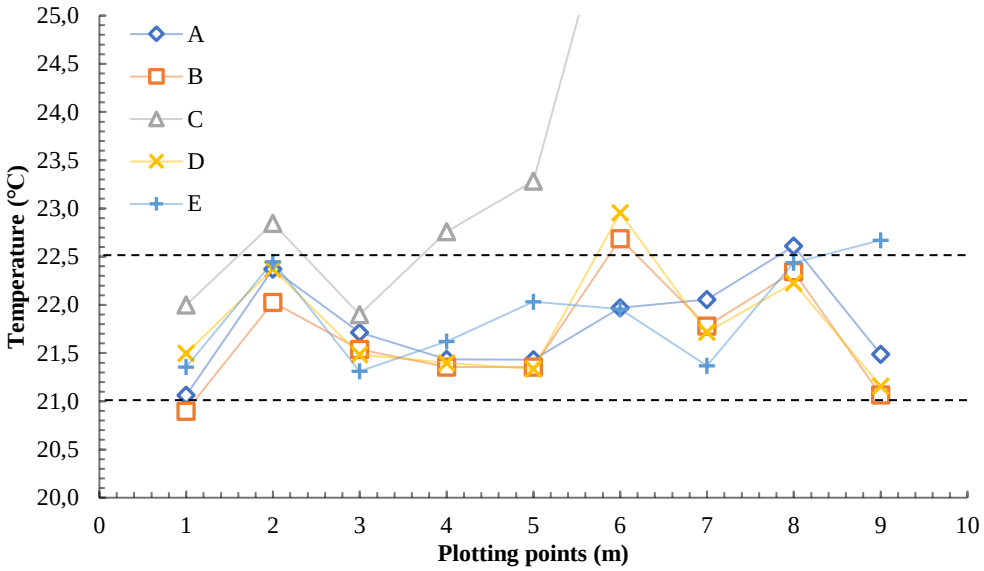

Fig. 12. Air temperature distribution in the executive passenger cabin

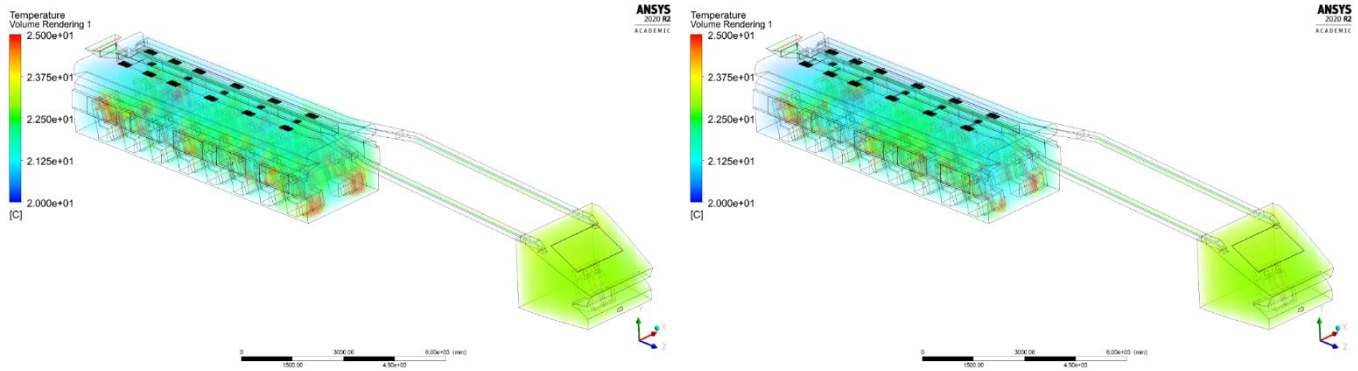

(a) (b)

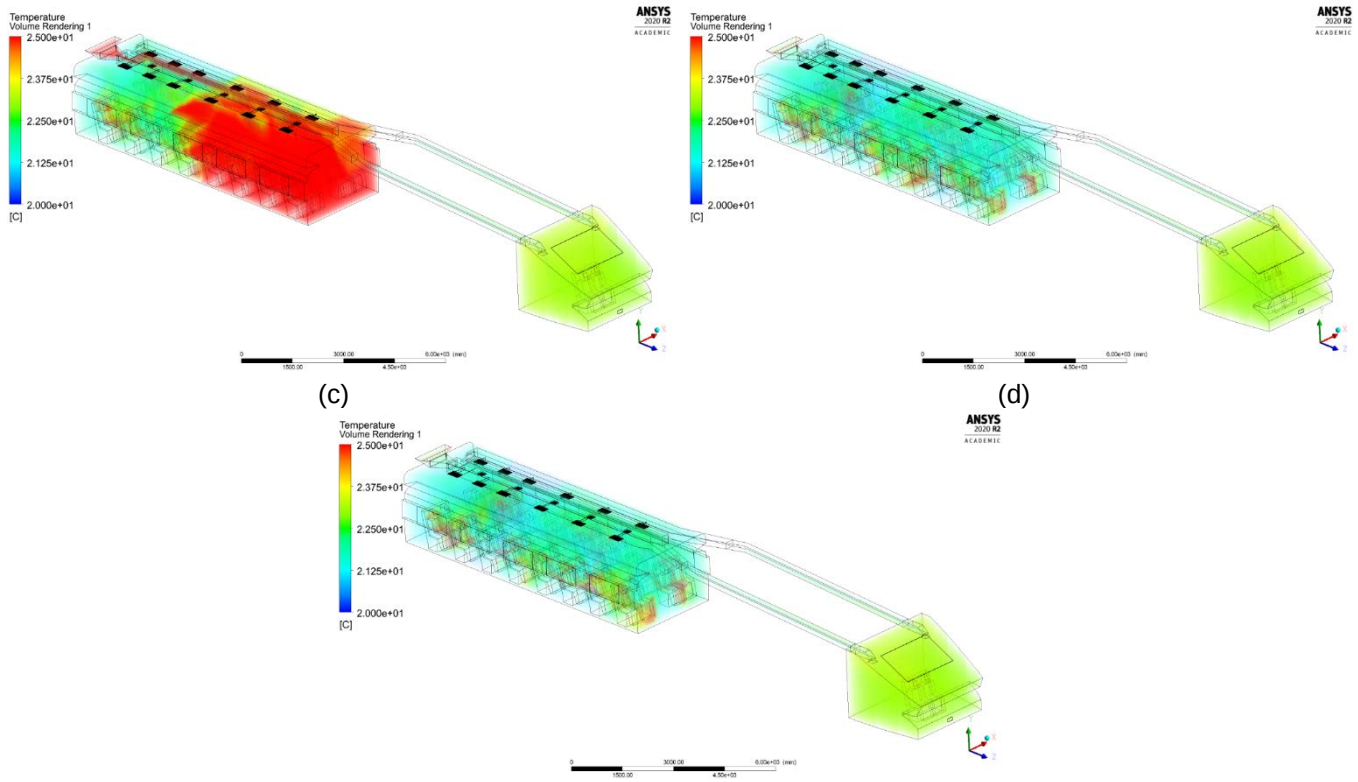

(c) (d)

(e)

Fig. 13. Isometric view of air temperature rendering for (a) variation A, (b) variation B, (c) variation C, (d) variation D, and (e) variation E

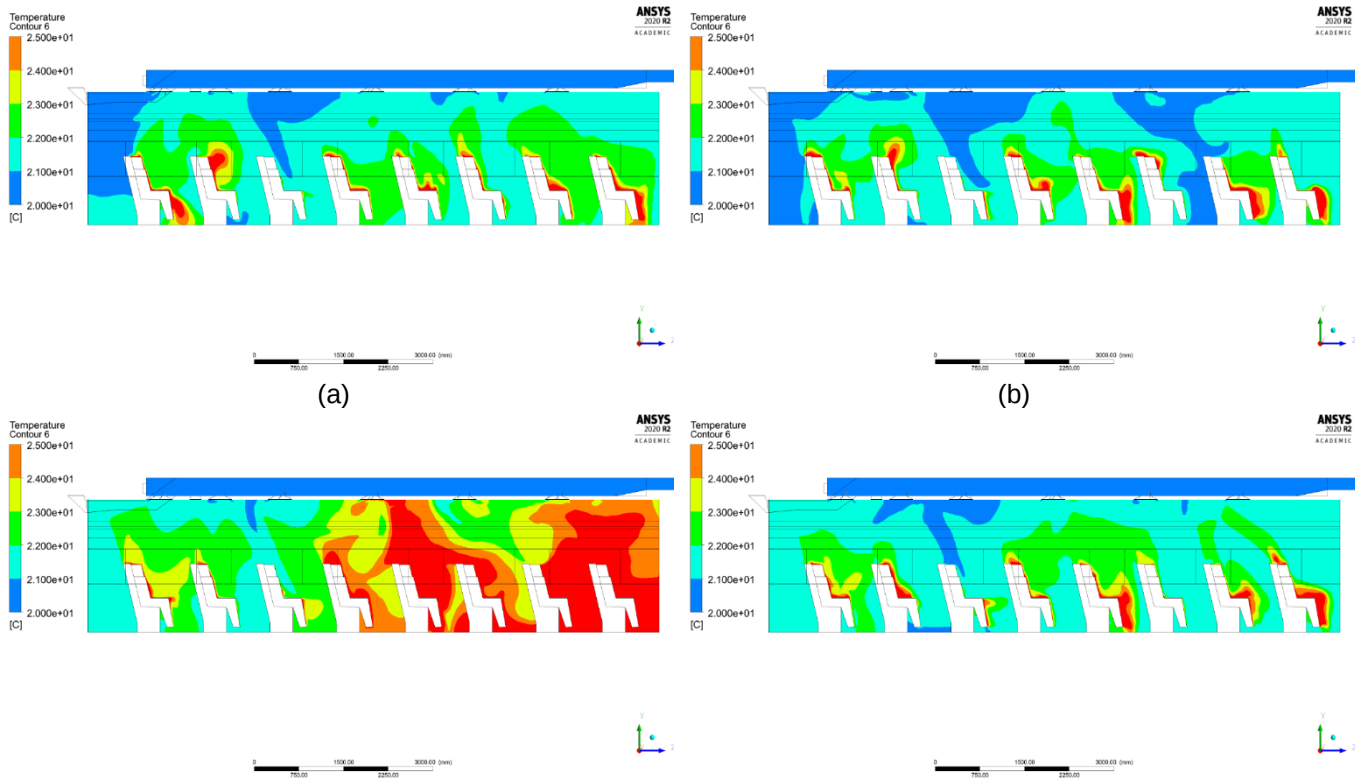

(a) (b)

(c) (d)

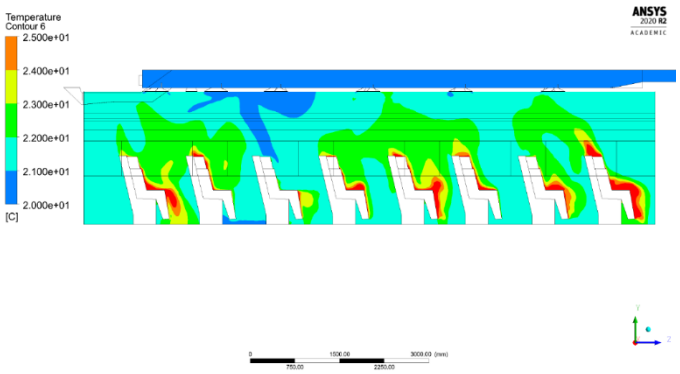

(e)

Fig. 14. Side view of air temperature contours for (a) variation A, (b) variation B, (c) variation C, (d) variation D, and (e) variation E

Figure 15 shows the air velocity vector of variation C and variation E on the plane of the passenger closest to the window. The authors wanted to compare these 2 variations which produced the worst and the best air temperature distribution in executive passenger cabin. The vector direction of air velocity will be analyzed to be able to explain why variation C can produce the worst air temperature distribution and the why the variation E can produce the best air temperature distribution.

These two variations C and E produced an air velocity vector that gathers a lot in the middle passenger seats, or at a plotting point of about 3 meters. In variation C in Figure 15 (a), the vector direction concentration occurred at the front passenger seat, or at a plotting point of approximately 7-8 meters. This rotation of the air velocity vector might cause of the high air temperature distribution in the front passenger seat in variation C. In variation E in Figure 15 (b), the air velocity vector on the front passenger seat, or at a plotting point of approximately 7-8 meters did not occur with an air velocity vectors rotation. This might cause the results of the air temperature distribution in the variation E to be more even than the variation C and produced the best air temperature distribution among the other variations.

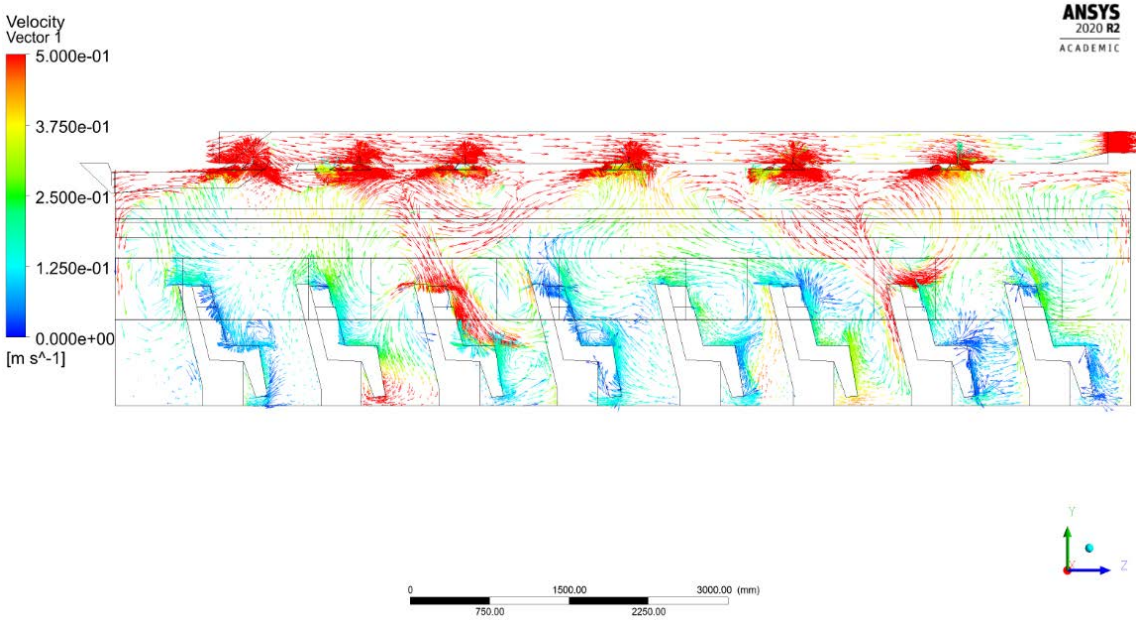

(a)

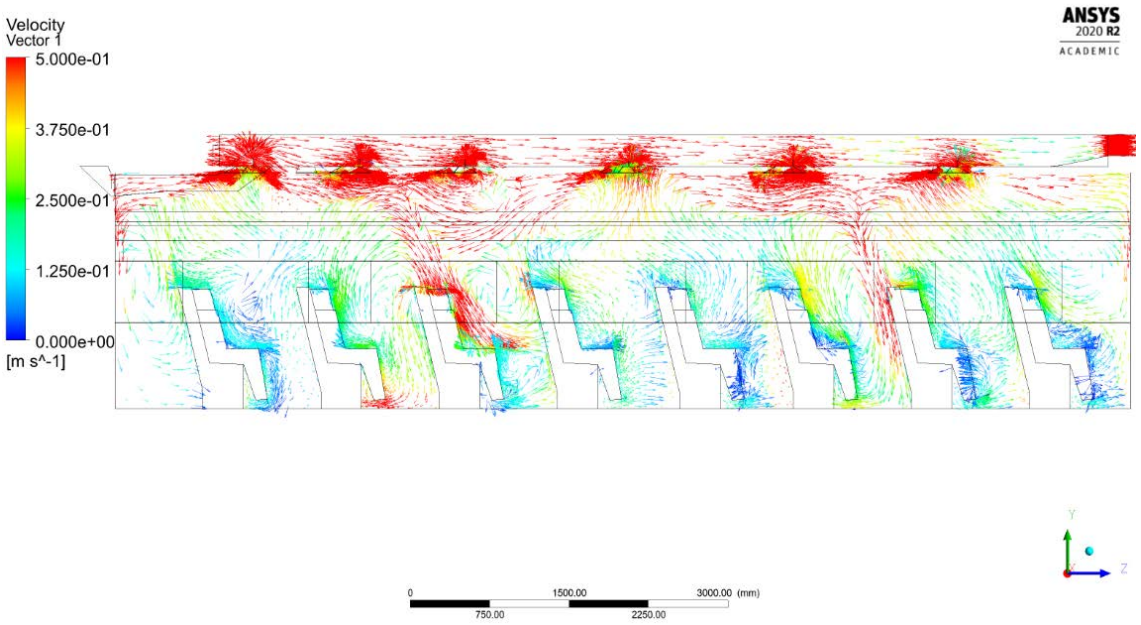

(b)

Fig. 15. Air velocity vectors on the passenger closest to the window for (a) variation C and (b) variation E

4 CONCLUSION

Through numerical analysis of the effect of variations in obstructions in the ducting on the distribution of air velocity and air temperature in the executive passenger cabin, it can be concluded that:

- Air barriers affected how the outgoing air flow was distributed in each diffuser at different distances from the flow source, especially with variations in the height of the barriers in each diffuser. It influenced the distribution of air velocity and temperature in the executive passenger cabin.
- Variations E had the best overall design with the average air velocity value is about 0.25 m/s which is below the standard of 0.5 m/s. Variation E also produced the average air temperature value in the executive passenger cabin of 21.91 °C, where the difference value in air temperature is 1.36 °C, which is below 1.5 °C and meets the regulation standard.

5 ACKNOWLEDGEMENTS

This research was the result of a project entitled Pengembangan dan Pembuatan Kereta Cepat Merah Putih with the grant number of 369/E1/KS.06.02/2022 which was funded by Kedaireka Matching Fund, Ministry of Education, Culture, Research, and Technology Indonesia, Year 2022 Batch 5.

6 REFERENCES

[1] Samah, H., Banna, M. (2009). Performance Analysis of Thermal Insulation Screens used for Classic Roofs in Hot-Humid Tropics. International Energy Journal, vol. 10, 255–266.

[2] Ratanachotinun, J., Pairojn, P. (2014). Feasibility Study of Glass Solar Chimney Wall for Tropical Area, Case Study: Bangkok, Thailand. International Energy Journal, vol. 14, 95–106.

[3] Peng, Y., et al. (2022). Passenger overall comfort in high-speed railway environments based on EEG: Assessment and degradation mechanism. Build Environ, vol. 210, 1–10, DOI: 10.1016/j.buildenv.2021.108711.

[4] Rugh, J., Bharathan, D. (2005). Predicting Human Thermal Comfort in Automobiles. Vehicle Thermal Management Systems Conference and Exhibition 2005, p. 1–9, DOI: https://doi.org/10.4271/2005-01-2008.

[5] Yang, A., et al. (2017). Numerical study on aerodynamic characteristics of high-speed trains with considering thermal-flow coupling effects. Journal of Vibroengineering, vol. 19, no. 7, 5606–5626, DOI: 10.21595/jve.2017.18778.

[6] Selamat, H., Hanif, M., Sharif, Z., Attaran, S., Sakri, F., Razak, M. (2020). Review on HVAC System Optimization Towards Energy Saving Building Operation. International Energy Journal, vol. 20, 345–358.

[7] Hesser, K., Widdowson, J. (2016). Guideline for the Design and Application of Heating, Ventilation, and Air-Conditioning Equipment for Rail Passenger Vehicles. ASHRAE, Atlanta.

[8] Menteri Perhubungan RI, Kementerian Perhubungan Republik Indonesia. Peraturan Menteri Perhubungan Republik Indonesia Nomor PM 69 Tahun 2019 Tentang Standar Spesifikasi Teknis Kereta Api Kecepatan Tinggi, from https://djka.dephub.go.id/uploads/202207/PM_69_TAHUN_2019.pdf, accessed on 2023-05-01.

[9] ANSYS. (2010). ANSYS Fluent Theory Guide, 13th ed. ANSYS Inc., Canonsburg.

[10] Ranjan, R., Paswan, M., Prasad, N. (2017). CFD Based Analysis of a Solar Air Heater Having Isosceles Right Triangle Rib Roughness on the Absorber Plate. International Energy Journal, vol. 17, 57–74.

[11] Samah, H., Tiwari, G., Nougblega, Y. (2020). Cool and Green Roofs as Techniques to Overcome Heating in Building and its Surroundings under Warm Climate. International Energy Journal, vol. 20, 359–372.

[12] Menter, F., Sechner, R., Matyushenko, A. (2021). Best Practice: RANS Turbulence Modeling in Ansys CFD, 1st ed. ANSYS Inc., United States of America.

[13] Khan, I., Baruah, M., Dewan, A., Mahanta, P. (2009). Computational Investigation of Energy Efficient Pin Fin Cross Section for a Compact Heat Exchanger. International Energy Journal, vol. 10, 233–246.

[14] Incropera, F. (2011). Fundamentals of Heat and Mass Transfer, 7th ed. John Wiley & Sons Inc., Jefferson City.

[15] Yusra, A., Haryanto, I., Jamari, D. (2008). Analisa Kontak Elastis Antar Hemispheres Menggunakan Metode Elemen Hingga. Rotasi, vol. 10, 3–7.

7 NOMENCLATURE

C_p	Specific heat, $\mathrm{J/kg\,K}$	$q"$	Heat flux, $\mathrm{W/m^2}$
E	Energy, J	S_h	Volumetric heat sources
$\vec{F}$	External body forces, N	$S_{k,\omega}$	Source term
g	Gravity acceleration, $\mathrm{m/s^2}$	S_m	Source terms for mass added
G_k	The forming of turbulence kinetic energy	T	Temperature, $\mathrm{°C}$
G_ω	Generation of specific dissipation rate	t	Thickness, m
h	Enthalpy, J	t	Time, s
h	Heat transfer coefficient, $\mathrm{W/m^2K}$	$\vec{v}$	Vector velocity, $\mathrm{m/s}$
I	Unit tensor	$Y_{k,\omega}$	Dissipation due to turbulence
J	Diffusion flux, $\mathrm{kg/m^2s}$	$\Gamma_{k,\omega}$	Effective diffusivity
k	Thermal conductivity, $\mathrm{W/m\,K}$	μ	Dynamic viscosity of the fluid, $\mathrm{kg/m\,s}$
k	Turbulence kinetic energy	ρ	Density of the fluid, $\mathrm{kg/m^3}$
$\dot{m}$	Mass flow rate, $\mathrm{kg/s}$	$\bar{\bar{\tau}}$	Tensor stress, $\mathrm{N/m^2}$
p	Pressure, $\mathrm{N/m^2}$	ω	Specific dissipation rate

Paper submitted: 10.07.2023.
Paper accepted: 20.09.2023.